EUROPEAN ORGANIZATION FOR NUCLEAR RESEARCH

CERN-PPE/93-170
6 September 1993

The CERES RICH Detector System

R. Baur[a], A. Breskin[b], R. Chechik[b], A. Drees[a], U. Faschingbauer[c], P. Fischer[a,1)], Z. Fraenkel[b], J. Gläß[a,2)], P. Glässel[a], C.P. de los Heros[b], D. Irmscher[a], R. Männer[a,2)], A. Pfeiffer[a], A. Schön[a], J. Schukraft[d], Ch. Schwick[a,3)], A. Shor[b,4)], H.J. Specht[a], V. Steiner[b], S. Tapprogge[a], G. Tel-Zur[b], I. Tserruya[b], Th. Ullrich[a], J.P. Wurm[c]

[a] Universität Heidelberg, Germany[5)]
[b] Weizmann Institute, Rehovot, Israel[6)]
[c] Max-Planck-Institut für Kernphysik, Heidelberg, Germany
[d] CERN, Geneva, Switzerland

Abstract

We describe the two RICH detectors of the CERES electron pair spectrometer at the CERN SPS which are used for electron identification and, in conjunction with a novel silicon drift detector, for tracking in pp, pA and AA collisions. The RICH detectors are operated at a high $\gamma_{th} \simeq 32$ (CH_4 at 1 atm.) and are thus rather insensitive to hadrons. The UV-detectors are multi-step counters with a multi-wire chamber as the last stage. They are operated at gains of $2 - 4 \cdot 10^5$ using a mixture of He + 6% C_2H_6 (or CH_4) + TMAE.

The two UV-detectors are equipped with 53 800 (48 400) square pads. The front end electronics consists of modules with 256 (121) channels, based on a 64-channel charge-sensitive preamplifier VLSI chip. The total readout time is 280 (1600) μs per event. Subsets of the pad data are used as input to a fast trigger processor selecting events with at least two separated electron rings. The trigger achieved an enrichment factor of ~ 100 in proton-induced interactions, and a factor of ~ 3 in ^{32}S - Au collisions.

The RICH detectors perform very close to their design values. We observe clean Cherenkov rings with an average number of 11.2 (12.5) photons/ring. This is consistent with the calculated value $N_0 = 131$ (75) cm^{-1} within the systematical error of about 10%. The spatial resolutions of 1.0 and 0.8 mrad (rms) for individual photons are dominated by chromatic aberration and in very good agreement with theoretical expectations.

to appear in the Proceedings of the First Workshop on RICH Detectors, Bari, Italy (1993)

---

1) now at Universität Bonn, Germany
2) now at Universität Mannheim, Germany
3) now at DESY Hamburg, Germany
4) now at Soreq Nuclear Research Center, Yavne, Israel
5) supported by BMFT under grant 06HD525I
6) supported by Minerva, the German Israeli Foundation and the Kadoorie Family Endowment Fund

1 Introduction

The CERES experiment (CErenkov Ring Electron Spectrometer) [1] studies the production of low mass e^+e^- pairs in proton-proton, proton-nucleus and nucleus-nucleus interactions at the CERN SPS. The acceptance covers the rapidity region $2.1 < \eta < 2.7$ and the mass region 100 MeV/$c^2 \lesssim m_{ee} \lesssim$ 3 Gev/c^2. Electron pairs (as well as photons and lepton pairs in general) are considered to be one of the best probes of the hot early stages of nuclear collisions due to the absence of final state interactions. However, the measurement of electron pairs is also very difficult. The main problem is the need to detect a relatively weak source, with a strength of $\simeq 10^{-5}$ e^+e^-/π°, in the presence of an overwhelming yield of e^+e^- pairs originating from trivial sources, like γ conversions and π° Dalitz decays. These background pairs must be recognized with a high efficiency to reduce the otherwise prohibitive combinatorial background.

CERES is the first experiment which measures e^+e^- pairs in nuclear collisions. The layout of the spectrometer is shown in Fig. 1. Particle identification and directional tracking in CERES is based on two azimuthally symmetric Ring Imaging Cherenkov (RICH) detectors, one (RICH-1) situated before, the other (RICH-2) after a superconducting double solenoid. A silicon drift detector before RICH-1 allows particle tracking to the interaction point. The RICH detectors are virtually "hadron-blind" as originally proposed in ref. [1], i.e. most of the charged hadrons do not produce photons, while essentially all electrons create Cherenkov rings of asymptotic radius. This is achieved by using CH_4 at atmospheric pressure as the radiator gas, which results in a Cherenkov threshold of $\gamma \simeq 32$.

The two superconducting main solenoids provide an azimuthal momentum kick between the two RICH detectors for momentum and charge analysis. The field in the region of RICH-1 is compensated to nearly zero using an asymmetry in the currents of the superconducting coils, preserving the information of the original direction of the particles. This allows the rejection of trivial pairs by applying cuts on the opening angle or number of hits per ring in RICH-1. A set of warm coils shapes the field in the RICH-2 radiator such that it points back to the target (see the field lines in the lower part of Fig. 1). The particle trajectories are thus parallel to the field lines and undeflected within RICH2 – except for a small second order deflection towards the beam axis –, an essential requirement for sharp ring images.

In order to minimize the number of e^+e^- pairs from conversions and to reduce the loss of momentum resolution due to multiple scattering, the amount of material within the acceptance is minimized. For this reason the mirror of RICH-1 is based on a carbon fiber laminate shell of only 1 mm thickness [2]. The second mirror is a conventional 6 mm glass mirror, assembled from 10 individual pieces. The target is segmented into many beam-size discs which keeps most of the target material out of the acceptance of the spectrometer. All in all, the total radiation length was kept at about 0.7% and 1.6% of X_0 up to the first and second mirror, respectively, excluding the target.

The Cherenkov photons from the RICH radiators are registered in two detectors which are placed upstream of the target, therefore they are not traversed by the intense flux of forward going particles (especially in nucleus-nucleus collisions). This implies that the target is not at the center of curvature of the mirrors but at a distance of about 40%

of the radius of curvature. As an additional benefit of this geometry, the focal planes are virtually flat. Both UV-detectors are built as multi-step gas counters operated with TMAE as the photo-sensitive agent [3]; drift and multiplication are perpendicular to the focal plane. In order to achieve high UV-photon conversion efficiency in the TMAE on the short distance necessary to keep the single electron diffusion at an acceptable level, the detectors are operated with TMAE vapor saturated at 40°C. To avoid condensation and temperature gradients, the whole spectrometer is heated to 50°C.

The information of the UV-detectors is read out via a two-dimensional array of pads [4, 5, 6] allowing the unambiguous reconstruction of single photon hits. A subset of the information of RICH-1 is used for pattern recognition in a fast higher-level trigger scheme.

CERES is the first experiment to use a silicon drift chamber. Its radial design has been described elsewhere [7, 8]. Situated close to the target, it serves as a high-resolution vertex detector free of ambiguities due to its intrinsic 2-dimensional operation. The prime purpose of the silicon drift chamber is to supply the additional rejection of conversion and Dalitz pairs necessary for sufficient reduction of the combinatorial pair background in nucleus-nucleus collisions [9]. Another silicon detector with azimuthal symmetry, segmented in 64 pads, provides fast multiplicity information used in the trigger [10].

The partially equipped spectrometer was first installed and tested at CERN in 1990. Further improvements on the UV-detectors were completed in 1991 and the fully equipped spectrometer with the present UV-detector scheme was successfully tested. Since 1992 large data samples have been collected for proton and ^{32}S beams, respectively.

This paper deals only with the RICH detectors. We give short accounts of the UV-detectors (Section 2), the pad readout (Section 3), the intelligent triggers based on the information of RICH-1 (Section 4), and finally we report on the performance of the RICH detectors. More detailed accounts of the CERES spectrometer in general, of the pad readout and the trigger are in preparation.

2 The UV-Detectors

The UV-detectors of RICH-1 and RICH-2, in the following called UV-1 and UV-2, are the crucial elements of the spectrometer. Their main properties are a high detection efficiency for UV-Cherenkov photons which requires operation at a gain $\geq 10^5$, and a good spatial resolution, quadratically small compared to the chromatic dispersion which is the main factor determining the high-momentum limit of the spectrometer resolution.

The first UV-detectors of the CERES spectrometer consisted of two-stage parallel-plate avalanche counters (PPAC) with a gate in between, a scheme adopted after a series of prototype tests [11, 12, 13]. This design had two attractive features: the multi-step scheme avoids photon feedback by absorption between the multiplication stages, and the PPAC structures are very robust mechanically. However, it became clear from the first beam tests in 1990, that the detectors could not be operated in the beam environment at the required gain of 10^5 due to a prohibitively high sparking rate [14]. After a series of lab tests, it was found that multi-wire proportional chambers (MWPC) are much less prone to sparks than PPAC structures operated at the same multiplication. (A detailed account of the spark problem and of the performances of MWPC vs. PPAC is given in [14]). The

detectors were then modified by adding a MWPC as a third amplification stage.

The present scheme is shown in Fig. 2. It consists of two PPAC stages with a gate in between, and a MWPC as a third stage. Photons enter through the entrance window and are converted in the 15 mm deep conversion gap. The conversion electrons drift towards the first amplification gap. The avalanche then propagates through the first transfer region towards the second PPAC where it is further amplified. (The – unused – gate and the PPAC are adjacent without a transfer region between them. This allowed to add the MWPC element keeping the total length of the detector unchanged and therefore to use the same detector housing). The two PPAC's are operated at very low gains of < 100 each. The avalanche finally drifts through the second transfer region towards the MWPC structure where the full gain of $2 - 4 \cdot 10^5$ is achieved. The electron avalanches at the wires of the MWPC induce positive charge signals on the last cathode consisting of a resistive layer, a dielectric, and the pad electrode used for the readout.

The time constant for charge movements in the resistive layer is large compared to the avalanche development time; the resistive layer is thus "transparent" to the signals [15]. The purpose of the resistive layer – as compared to ordinary cathode pads – is that both the entrance window, and the pads, which are connected to the front end electronics, can be kept at ground potential.

The main difficulty in the construction of the detectors is due to their large size. They have an annular shape with inner/outer active diameters of 280/784 mm (1068/2182 mm). (Here and in the following the respective numbers for UV-2 will be given in parentheses). The parallel plate electrodes were manufactured in one piece in order to benefit from the mechanical stability inherent to the circular geometry. They are made of stainless steel meshes with 50 μm wire diameter and 500 μm pitch, glued on two concentric rings made of G10. There are no spokes connecting the two rings, thus the rings keep the tension of the mesh and in turn the tensioned mesh keeps the rings concentric. The electrode at the window has 30 μm wire diameter to increase transparency. The multi-wire stage has a mesh cathode at the entrance, which is identical to the parallel plate electrodes. The anode plane consists of wires of 30 μm diameter with a spacing of 2 (3) mm; it is divided azimuthally in 10 (16) sectors by radial spokes connecting the inner and outer frame. The spokes are needed both for the wire geometry (the wires are parallel to the central radius within each sector), and to give the frame enough mechanical stability (the wires are much more fragile than the meshes).

The last cathode is a sandwich structure consisting of a resistive layer of 130 M$\Omega/\square$ [16], a dielectric made of G10 of 0.6 (2.6) mm thickness, and the pad electrode. The square pads have a pitch of 2.74 mm in UV-1 and of 7.62 mm in UV-2, so that 53 800 (48 400) pads are needed to cover the total active area of 0.42 (2.84) m^2. For the chosen geometry, one pad in the focal plane corresponds to an angle of 2.19 (1.82) mrad (the asymptotic Cherenkov ring radius is about 14.5 (16.5) pads).

The UV-detectors were initially operated at atmospheric pressure with He + 6% C_2H_6 + TMAE saturated vapor at 40°C. Great care was taken to have a very clean system not containing any materials attacked by TMAE. Gas tightness was carefully checked and residual O_2 was required to be at the ppm level before admitting TMAE. With these precautions, TMAE operation did not cause any problems. Since 1993, 6% CH_4 is used as the quencher for its higher UV-transparency with no adverse effects of any kind. The

performance of this scheme in the beam environment is very satisfactory. The detectors are typically operated at gains of $2 - 4 \cdot 10^5$, with proton and ^{32}S beam intensities up to 10^7 particles/burst, and with interaction rates of a few percent of that. The spark rates are so low that the gating of the chambers used in the initial scheme, which in other respects (pickup in the silicon counters) is not unproblematic, was abandoned. In the ungated mode we now observe spark rates (all of them occurring in the PPAC's) of the order of about one every second burst, i.e. a spark probability of order 10^{-5}/interaction for proton and ^{32}S beams. In the proton case, most of the sparks are not even associated with target interactions, but with upstream interactions of the beam and with shower particles traversing the UV-detectors almost parallel to the drift direction and thus projecting the whole 15 mm long track onto a small spot.

The UV-photon mean free path in TMAE at 40°C, averaged over the bandwidth of the RICH, was found to be 6.6 mm [17], in good agreement with the published value of 7 mm at 170 nm [18]. The 15 mm conversion gap ensures therefore a 90% photo-conversion efficiency. The high gain operation of the chamber together with the low threshold in the readout electronics results in a 92% single electron detection efficiency. Fig. 3 shows a pulse height spectrum of single UV-photon hits in UV-1. It exhibits the exponential distribution of single-electron avalanches expected for operation well below the photon feedback threshold. The average gain, given by the inverse slope, is $2.3 \cdot 10^5$.

The shape of the induced signal on the pads is approximately Gaussian. Its width is determined by the geometry. With the chosen anode-to-cathode gap distance of 2 (4) mm and the thickness of the G10 dielectric (limited in UV-1 by mechanical considerations), the width of 0.81 (0.63) pads (rms) in one dimension is somewhat larger than the optimum for position interpolation and double-hit resolution, but still quite adequate. The signal of a single-electron avalanche is therefore seen on a few neighboring pads (the hit profile can be seen in Fig. 11 below). The interpolation between pads by the center-of-gravity method gives a readout accuracy of about 0.1 to 0.15 pads.

A detailed account of the design, construction and performance of the UV-detectors is contained in ref. [17]; a paper is in preparation.

3 The Pad Readout Electronics

The analog pulse height of each pad is read out by modules specially developed for this purpose [4, 5, 6]. They are based on the CAMEX [19] VLSI chip which has 64 charge-sensitive preamplifiers and was originally developed for silicon detectors. During the well-defined time interval in which the electron avalanches reach the amplifying wires ($2.1 \leq t \leq 4.4$ μs), the chips are activated externally and the charge signals of all channels are stored on the chips. This gated mode of operation makes the readout insensitive to off-time background. However, an external trigger is required to start the charge integration. Table 1 lists the important parameters of the pad readout, Fig. 4 shows a schematic block diagram of the readout electronics of RICH-1. More details are given in refs. [6, 20, 21].

The modules are directly plugged onto the pad plane. Each of them (Figs. 5 and 6) contains 8×32 (11×11) charge-sensitive channels, with a total of 210 modules on UV-1 and 400 on UV-2. Each channel has an external two-way diode protection circuit at the

input which was found to be necessary under sparking conditions. The first generation of modules which was unprotected suffered from continual channel losses; for the present, protected modules, no losses due to sparks are observed.

The RICH-1 module consists of 4 subcards which are identical except for the one card carrying the module readout (see Fig. 5). This allows the analog summation of pads on the module, a feature used for the intermediate-level trigger (Section 4.2). The pedestals of the amplifiers are individually corrected by analog subtraction using a digital-to-analog converter and digital pedestals stored on the module, and the corrected amplitudes are sequentially digitized (8-bit) on the module. The digitized information of up to 15 modules (=3840 channels) is transferred sequentially via about 45 m long twisted pair cable at a speed of 14 MHz to buffer FIFO modules located in the counting room. There are 16 of these "chains" read out in parallel so that the total readout time is 280 μs. (The special readout sequence for the intermediate-level trigger data, see Section 4.2 below, adds another 18 μs).

The RICH-1 pad electronics described above is the second generation which was introduced in order to speed up the readout and improve the performance of the trigger (see next Section). RICH-2 is still equipped with the first generation. There, the pedestal correction and digitization of the amplitudes are not done on the module, rather the analog pulse heights are multiplexed and sent to 14 chains which are read out in parallel at the lower speed of 2.5 MHz with a total readout time of 1600 μs. The pulse heights are corrected for pedestals and digitized in ADC's located in the counting room within the buffer modules.

The digitized information of the two counters then undergoes zero-suppression with individual thresholds for each channel, and it is finally stored together with a channel and chain label in a FIFO memory. The FIFO is unloaded at 20 MHz by the Fast Data Collection System (FDCS) [6, 20], a custom bus with a pipe-line structure. All further processing is done by VME modules on this bus.

The zero-suppression reduces the amount of data to 500 – 4000 words per event, depending on the type of events. For typical pad occupancies well below 1/16, the FIFO's of the chain buffers are always nearly empty, and the FDCS sequence is finished right after the end of the chain readout sequence.

At a sensitivity of 2700 (2200) electrons per ADC count, the average rms noise is 1800 (2500) electrons equivalent noise charge. A large contribution to these figures is due to the least-significant-bit noise of both the ADC's and the digital-to-analog converters used for the analog pedestal subtraction. At a detector gain of $2 \cdot 10^5$ the signal-to-noise ratio is typically about 30 or more for the mean pulse height of the central pad of a photon hit, resulting in a high detection efficiency of $\gtrsim 90\%$ for the single-electron avalanche signals. For the 8-bit ADC's, the dynamic range is about $2 \cdot 10^6$ electrons per avalanche.

The amplifier chips are sensitive to static discharges which caused some losses during the module assembly, but once the diode protection circuit was connected, no further losses were observed. The initial fraction of about 1.5 (2.5)% of unusable channels remained essentially unchanged after more than 10 months of detector operation.

4 The Trigger

We have developed an intelligent second-level trigger (SLT) which is able to select events with interesting pairs of rings. This was possible only because of the relatively clean events observed in our hadron-blind RICH counters. The need for such a trigger is obvious since the interesting e^+e^- pair candidates have a very low production probability ($\sim 10^{-5}$ e^+e^-/π°). The trigger exploits the fact that they have a large opening angle leading to two isolated Cherenkov rings, whereas the abundant background of conversion and π°-Dalitz pairs predominantly results in close ring pairs. The trigger operates only in RICH-1, since there the low-mass pairs are not yet opened by the magnetic field.

For ^{32}S-induced reactions, the SLT performs pattern recognition on a subset of the UV-1 pads, and the trigger decision is available after 140 μs. For proton-induced reactions, there is an additional intermediate-level trigger (ILT), which is also based on pattern recognition on the UV-1 pad data, but on a faster time scale of 35 μs with a coarser granularity. This trigger exploits the fact that in proton-induced interactions the RICH detectors are virtually empty for most events, so the requirement of two separate electron rings of any kind is an efficient preselection. For ^{32}S-induced reactions, the granularity of the ILT is too coarse to cope with the substantially higher single-hit and ring density.

In the following we will give a short description of the intermediate and second-level triggers, for didactic reasons starting with the latter. A more detailed account of these triggers is in preparation.

4.1 The Second-Level Trigger

The basic idea underlying the pattern recognition algorithm of the SLT is a Hough transformation performed on the pad image [22, 23]. For each pad with a signal above a given threshold, a point-to-ring transformation is made with a ring diameter equal to the asymptotic ring diameter of electron rings. In the transformed image, an electron ring in the pad image leads to a peak. This is illustrated for the two electron rings shown in Fig. 11. In Fig. 7 (top), the digital image used by the SLT is displayed, obtained from every second pad both in the x and y-coordinate and applying a threshold. Fig. 7 (bottom) shows the transformed image, after the point-to-ring transformation. One clearly sees the two maxima corresponding to the two ring centers. The Hough transformation is equivalent to counting the hits in a circular mask (of the diameter of the desired rings) for each potential ring center.

As mentioned in Section 3, a subset of the pad data is diverted in the FDCS to the trigger processors. The random access readout feature of the CAMEX chip [19] is very advantageous here, since it allows to read these channels first, reducing the time needed to transfer the SLT input data to one quarter of the total pad readout time, i.e. to 70 μs.

The processor is organized as a systolic array of 160×176 identical processor elements, each treating a 1-bit pixel [24, 25, 26]. The semi-custom VLSI chip containing 8×8 of these processors was developed in 2 μm CMOS standard cell technology [24].

The processor elements are interconnected as a two-dimensional matrix; the VLSI chips are mounted on four boards of 1.2×1.2 m^2 size, containing 10×11 chips each. The boards are interconnected as a cylinder to allow shifting of the stored image along one axis without

boundary problems. In this way, it is possible to read out the array non-destructively by shifting the picture around the cylinder once. All processor elements operate in parallel at 25 Mips with identical control signals supplied by the sequencer, a RAM containing the microprogram instruction list loaded via VME. The processor elements basically contain two 1-bit pixel registers for the initial image, intermediate and final results, and a 6-bit counter which is used to accumulate the point-to-ring transformation. The image can be shifted in x and y-direction.

The trigger algorithm – typically less than 1000 instructions –, takes less than 40 μs processing time. It consists of four steps: removal of clusters not due to Cherenkov photons, identification of Cherenkov rings of fixed, asymptotic radius, elimination of close pairs, and counting the remaining rings. The removal of clusters, which are due to charged particles traversing the photon detector, was found to be rather important for the performance. Such clusters are recognized as extended, connected groups of set pixels. For each 5×5 pixel environment, the set pixels are counted, and those environments exceeding a threshold count are cleared. The mask used in the ring-finding algorithm is shown in Fig. 8. It is more sophisticated and also more efficient than the mask used to generate Fig. 7 (bottom) as it has a positive correlation region at the asymptotic Cherenkov ring diameter and a negative portion farther away from this diameter. The correlation is computed in parallel by shifting the input image along the circular path representing the mask, incrementing – or decrementing – in each step the counters that meet a set pixel. The mask rejects conversions to some extent by its negatively counting parts since the softer partner of the pair frequently leads to hits diffusely scattered around the ring of the stiffer partner. The few pion rings, which mostly have non-asymptotic diameters, are also rejected to some extent. After the transformation, local maxima above a chosen threshold are isolated and stored. The new intermediate image now contains the centers of all well-defined electron ring candidates.

In the next step, spatially resolved candidate rings closer than a required minimum distance are deleted rejecting mostly π°-Dalitz and conversion pairs. In the last step, a trigger signal is generated if there are ≥ 2 isolated ring centers. In case of a negative trigger decision, the pad readout and all other readout is aborted, the total dead time for such aborted events is 130 μs.

The trigger algorithm was developed and trained with multiplicity-triggered RICH-1 data from p+Au and ^{32}S+Au interactions. The rejection of events *not* containing a signal was optimized on data, whereas the signal efficiency was optimized using data events with added Monte Carlo signal ring pairs. The trigger was first used in the 1992 ^{32}S running, where an efficiency of $\sim 50\%$ and a rejection of ~ 6, i.e. a sample enhancement of 3 was obtained (at that time, the RICH-1 readout frequency was only 2.5 MHz). For the proton running in 1993, an efficiency of $\sim 70\%$ and a rejection of a factor $\gtrsim 120$ was achieved, with the very substantial sample enrichment $\gtrsim 80$.

For the future, we are considering using the SLT processor for RICH-2 as well, improving the selectivity by requiring a correlation of rings in RICH-1 and RICH-2 in a limited deflection range, i.e. by employing the momentum cut now used offline at the trigger level. In this case, the RICH-2 electronics will be upgraded to the faster readout of RICH-1.

4.2 The Intermediate-Level Trigger

Except for the coarser granularity, the philosophy of the ILT algorithm is similar to that of the SLT: clusters are removed, rings are identified and counted. There is no distance criterion between rings.

One ILT pixel corresponds to 8×8 original pads, i.e. 16 times coarser granularity than the SLT pixels. The pulse height information used for these ILT pixels is obtained by summing pads. An analog sum of every second pad out of the RICH-1 module width of 8 pads (called a strip), i.e. of four pads, is done on the module by simultaneously addressing them on the four subcards (see Section 3). Four of these strips representing 8×8 pads are read out first in the pad readout channel sequence and are passed through the zero-suppression and FIFO's of the buffer modules like ordinary pad channels; in the FDCS chain they receive special xy-addresses from a xy-lookup module. The ILT interface diverts these pad amplitude data to the ILT summing module where they are summed on-the-fly into a memory. Whenever this sum exceeds a chosen ILT pixel threshold, the xy-address is passed from the summing module to the ILT processor memory, setting the corresponding ILT pixel. After the readout of all strips, the ILT processor itself is started. Here, because of the relatively small number of 36×36 pixels, the algorithm does not operate in parallel on the whole matrix as for the SLT, but treats the image line-by-line. Each line of pixels is fed to two rows of 36 processor elements each, which are connected in pipeline mode. The first row does the cluster removal, the second the ring pattern recognition, the output goes to a decision and storage module. A trigger is generated whenever the number of ring candidates is ≥ 2, otherwise the readout is aborted. The total decision time of the ILT (including the abort of the readout sequence) is 35 μs, dominated by the readout time of 18 μs, the electron drift time and the analog storage on the CAMEX chip (9 μs). The time to process the algorithm is only about 1.5 μs. The whole processor, based on programmable logic cell arrays (XILINX LCA), fits on three VME cards.

In the proton running, for various targets, this trigger gave reduction factors of 5 to 7 with a signal efficiency of 90 to 95%. Compared to the second-level trigger alone, the combined two-level scheme enhances the data sample by another factor of about 2.

5 Performance of the System

An example of a p+Be event is presented in Fig. 9 demonstrating the cleanliness of the RICH information. In addition to photon hits that are clearly associated with Cherenkov rings, there is a very low background of scattered single hits. Sources for such hits are pions just above threshold and low energy electrons either close to the threshold or undergoing large multiple scattering. The situation is quite different in a central S+Au collision as shown in Fig. 10. The background there is much more severe, but the pad occupancy is still at a relatively low level of about 5% for S+Au central collisions. Both in the proton and the ^{32}S-data, the number of UV-photon hits – on rings or not – is found to vary linearly with the event multiplicity. Apart from such single photon hits, due to pions and δ-rays, one observes clusters due to charged particles. Those coming from the target produce (i) diffuse spots due to the production of Cherenkov light in the window

material and (ii) short intense tracks due to dE/dx, if they traverse the conversion gap. There are also occasionally particles from showers occurring upstream and traversing the UV-detectors. The recognition of the clusters is no problem for the pattern recognition; the dead area per event, due to their rejection, is not significant.

Fig. 11 is an enlargement of the π^0-Dalitz pair of Fig. 9, exhibiting the details of the hit structure as seen by the pads. One notices the large dynamic range of hit amplitudes, due to their exponential distribution.

All in all, the UV-detectors have been operated for a total of about 10 months in the present configuration without opening the detectors once. No noticeable decrease of the gas gain due to ageing has been noticed in this period.

5.1 Photon Yield

The average number of photoelectrons N in an asymptotic ring for a radiator of length L is given by $N = N_0 \cdot L/\gamma_{th}^2$. N_0 is the figure of merit of the Cherenkov counter, obtained by folding the quantum efficiency of TMAE with the UV-transmission of the radiator gas, the detector gas and the UV-windows over the sensitive band width of the detector. RICH-2 is sensitive between 5.4 eV and 7.4 eV, i.e. between the ionization threshold of TMAE and the quartz window cut-off. RICH-1 has a CaF_2 window. Its upper cut-off is therefore higher and given by the detector gas (8.1 eV in the case of 6% C_2H_6). The larger bandwidth of RICH-1 results in a larger N_0 which allows to compensate for its shorter radiator length. The theoretical values of N_0 are 229 (135) cm^{-1} using the TMAE quantum efficiency from ref. [27] (about 10% higher values in the relevant wavelength band have been reported in ref. [28]). This figure gets degraded by other energy-independent photon losses, like the mirror reflectivity, first mesh transparency etc. All these losses are summarized in Table 2 and result in an effective figure of merit N_0^{eff} of 131 (75) cm^{-1}. The expected number of photoelectrons/ring is then 11.8 (12.5). The experimental number can be determined in several ways, all listed in Table 2: (i) from reconstructed δ-rays in otherwise empty events, taken with a special trigger. These rings are non-asymptotic in radius and rather diffuse due to multiple scattering. The hits are therefore subject to very little pile-up losses from the finite double-hit resolution of about 1.3 pads. The result is scaled to the asymptotic radius. (ii) N can be derived for normal rings, selecting reconstructed resolved Dalitz pairs in RICH-1 to avoid the abundant very close double rings that are not resolved by the analysis. Fig. 12 shows the distributions obtained for S+Au, with $N \simeq 9.5$ (10.5). In this case the pile-up losses are about 15 - 20% in both UV-detectors. (Residual contributions from unresolved double rings and the non-linear behavior of the pile-up modify the upper tails of the distributions). (iii) The third method is based on the pad pulse height summed over the ring area, divided by the mean amplitude/hit derived from isolated hits generated with a pulsed UV-lamp. The average of the three methods, correcting (ii) for the pile-up losses, is 11.2 (12.5) photons/ring. Given the estimated uncertainties of $\lesssim 10\%$ both on the observed values *and on the prediction*, the averages are is in remarkable agreement with expectation.

Recently, we have changed the counter gas to He + 6% CH_4 + TMAE, in order to profit in UV-1 from the higher UV cut-off of CH_4 as compared to C_2H_6 . The detectors work equally well with this mixture. The same gains are achieved at somewhat lower high

voltage. In UV-1, as expected, N increases by about one photoelectron.

5.2 Single-Hit Resolution

The momentum and mass resolutions of the spectrometer depend on the ring center resolution σ_θ which itself depends on the single UV-photon hit resolution σ_h as $\sigma_\theta = \pi\sigma_h/2\sqrt{N-2}$. The latter has a momentum-dependent contribution due to the multiple scattering. The momentum independent contributions are the chromatic dispersion, the mirror quality, the single electron diffusion in the conversion region and the readout accuracy (including the effect of the discreteness of the anode wires in the MWPC). All contributions are listed in Table 3 yielding a total single hit resolution of 1.08 (0.69) mrad in the high-momentum limit i.e. without multiple scattering. Fig. 13 shows the distribution of the distance of the hits from the fitted ring center for asymptotic rings. The data were taken from tracks with a momentum $p > 1$ GeV/c and belonging to fully reconstructed Dalitz pairs with separated ring fits in order to avoid the problem of the abundant conversion pairs which are often so close that the two rings are not resolved, resulting in an apparently worse resolution in RICH-1. The measured single-hit resolution σ_h, i.e. the rms scatter of the distribution in Fig. 13 is 1.02 (0.78) mrad in very good agreement with the expected values. These single-hit resolution figures imply a pair-mass resolution e.g. in the ϱ/ω region of about 10% (rms). The single-hit resolution is important for CERES in another respect. The resolution on the ring radius is $\sigma_r = \sigma_h/\sqrt{N-2}$, it is decisive for the discrimination between electrons and high-momentum pions. In the present offline analysis, pions can be separated up to about 15 GeV/c lab momentum.

6 Summary

We have described the RICH detectors of the CERES spectrometer. The UV-photon detectors are operated in a three-stage amplification mode consisting of two PPAC's and a MWPC which was found to be essential in order to cope with the large dynamic range from single electrons to nearly 10^4 electrons from slow particles. The detectors are operated with a mixture of He + 6% C_2H_6 (or CH_4) and saturated TMAE vapor at 40°C in DC mode and at gains of $2 - 4 \cdot 10^5$.

The fast pad readout together with the possibility to operate on subsets of the pad information has made ring recognition possible at the trigger level. Substantial enhancements of the sample are achieved both for proton and ^{32}S-induced interactions.

The efficiency to detect a converted photon in the UV-detectors is above 90%. The two RICH counters perform very close to theoretical expectations. We observe yields of about 10 resolved photons per Cherenkov ring, and single hit resolutions of 1.0 (0.8) mrad, both in close agreement with the calculated values.

Tables

Table 1

Specifications of the Pad Readout

	RICH-1	RICH-2
UV-detector area m^2	0.42	2.84
pads	53800	48400
pad pitch mm	2.74	7.62
channels per module	8×32	11×11
number of modules	210	400
readout chains	16	14
transferred information	digital	analog
max channels/chain	3840	4096
readout frequency MHz	14	2.5
total readout time μs	280	1600
cost per channel DM	5	4

Table 2

Cherenkov Photon Yield

S+Au data, counter gas He + 6% C_2H_6 + TMAE

		RICH-1	RICH-2
N_0 starting value	cm^{-1}	229	135
mirror reflectivity		0.85	0.85
transmission first mesh		0.89	0.89
absorption in 15 mm TMAE (40°)		0.90	0.90
radiator transmission		0.98	0.96
window spoke losses		0.93	0.93
electronic threshold		0.92	0.92
N_0^{eff}	cm^{-1}	131	75
γ_{th} (measured*, CH_4 50° 0.946 atm)		31.6	32.55
radiator length L_{eff}	cm	90	175
N expected		11.8	12.5
N observed (resolved hits, δ-rays)		10.0	11.4
N observed (resolved hits)		9.5	10.5
N observed (summed amplitude)		12.1	13.5

* The calculated γ_{th} is 3.4% (2.5%) larger.

Table 3

Contributions to the Single-Hit Resolution

rms in (mrad)

	RICH-1	RICH-2
chromatic aberrations in CH_4	0.95	0.53
readout (including discrete anode wires)	0.33	0.25
single electron diffusion	0.37	0.11
mirror quality	<0.10	0.35
total	1.08	0.69
observed value	1.02	0.78

Figure Captions

Fig. 1 Cross-sectional view of the CERES spectrometer. In the lower part, magnetic field lines are shown in the acceptance.

Fig. 2 Layout of the UV-photon detectors: two parallel plate stages and a final multi-wire stage. The gate is not used. The dimensions in parentheses refer to UV-2.

Fig. 3 Distribution of photon hit amplitudes in UV-1. The amplitudes are summed over 3×3 pads, centered on the maximum.

Fig. 4 Schematic block diagram of the RICH-1 pad readout and its interfacing to the trigger processors (see Section 4)

Fig. 5 The RICH-1 pad readout module

Fig. 6 The RICH-2 pad readout module

Fig. 7 Input image of the second-level trigger processor (top), and the result of a Hough transformation, exhibiting maxima at the ring centers (bottom).

Fig. 8 The pixel mask used for the ring correlation of the second-level trigger. The central part of the mask shown in black counts positively, the inner and outer pixels count negatively.

Fig. 9 A p+Be event with a pair due to a π^0-Dalitz decay

Fig. 10 A typical ^{32}S+Au event

Fig. 11 Enlarged view of the Cherenkov rings of Fig. 9 in UV-1. The areas of the little boxes are proportional to the pad amplitudes. The best-fit rings and centers determined offline are overlaid.

Fig. 12 Distribution of number of photons per ring in UV-1 and UV-2 from S+Au data (He + 6% C_2H_6 + TMAE). The smooth curves are Poisson distributions with the quoted means. A minimum of 7 hits is required per ring.

Fig. 13 Radial distribution of photon hits referred to the fitted ring centers (S+Au data). In UV-1, resolved Dalitz pairs have been selected. The flat contribution under the peaks is due to the close partner rings, and to single-hit background.

References

[1] U. Faschingbauer, M.G. Trauth, J.P. Wurm, A. Drees, P. Fischer, P. Glässel, M. Guckes, D. Irmscher, L.H. Olsen, A. Pfeiffer, H. Ries, A. Schön, H. Sickmüller, H.J. Specht, T.S. Ullrich, E.F. Barasch, A. Breskin, R. Chechik, Z. Fraenkel, D. Sauvage, V. Steiner and I. Tserruya, Proposal to the SPSC, CERN SPSC/88-25/P237 and SPSC/88-40/P237/Add.1

[2] Developed by MAN Technologie, München, Germany. To be published

[3] G. Charpak and F. Sauli, Nucl. Instr. Meth. **225** (1984) 627

[4] P. Fischer, A. Drees, P. Glässel, G. Lamade, H. Ries, A. Schön, H.J. Specht, A. Breskin, R. Chechik, Z. Fraenkel, D. Sauvage, V. Steiner, I. Tserruya and R. Horisberger, IEEE Trans. Nucl. Sci. **NS-35** (1988) 432

[5] P. Fischer, Diploma Thesis, Heidelberg 1988

[6] P. Fischer, Doctoral Thesis, Heidelberg 1992

[7] W. Chen, H. Kraner, Z. Li, P. Rehak, E. Gatti, A. Longoni, M. Sampietro, P. Holl, J. Kemmer, U. Faschingbauer, B. Schmitt, A. Wörner and J.P. Wurm, IEEE Trans. Nucl. Sci. **NS-39** (1992) 619

[8] W. Chen, H. Kraner, Z. Li, P. Rehak, G. Bertuccio, E. Gatti, A. Longoni, M. Sampietro, P. Holl, J. Kemmer, U. Faschingbauer, F. Hess, C. Jacob, A. Wörner, J.P. Wurm, R. Baur, A. Drees, P. Fischer, P. Glässel, T.F. Günzel, D. Irmscher, L. Olsen, A. Pfeiffer, B. Schmidt, A. Schön, H.J. Specht, Th. Ullrich, S. Tapprogge, N. Wermes, A. Breskin, R. Chechik, C. de los Heros, V. Steiner and I.Tserruya, Nucl. Instr. Meth. **A326** (1993) 273

[9] U. Faschingbauer, Doctoral Thesis, Heidelberg 1993

[10] T.F. Günzel, H.T. Nägele, A. Drees, U. Faschingbauer, P.Fischer, D. Irmscher, L. Olsen, N. Wermes and J.P. Wurm, Nucl. Instr. Meth. **A316** (1992) 259

[11] A. Drees, P. Fischer, P. Glässel, G. Lamade, H. Ries, E. Schmoetten, H.J. Specht, A. Breskin, R. Chechik, Z. Fraenkel and I. Tserruya, Nucl. Instr. Meth. **A273** (1988) 793

[12] A. Breskin, R. Chechik, Z. Fraenkel, D. Sauvage, V. Steiner, I. Tserruya, G. Charpak, W. Dominik, J. P. Fabre, J. Gaudaen, F. Sauli, M. Suzuki, P. Fischer, P. Glässel, H. Ries, A. Schön and H.J. Specht, Nucl. Instr. Meth. **A273** (1988) 798

[13] A. Breskin, R. Chechik, A. Drees, P. Fischer, Z. Fraenkel, P. Glässel, G. Lamade, H. Ries, D. Sauvage, A. Schön, E. Schmoetten, H.J. Specht, V. Steiner and I. Tserruya, IEEE Trans. Nucl. Sci. **NS-35** (1988) 404

[14] R. Baur, A. Drees, P. Fischer, Z. Fraenkel, P. Glässel, H. Klein, A. Pfeiffer, A. Schön, A. Shor, H.J. Specht, V. Steiner, I. Tserruya and T.S. Ullrich, these proceedings

[15] G. Battistoni, P. Campana, V. Chiarella, U. Denni, E. Iarocci and G. Nicoletti, Nucl. Instr. Meth. **202** (1982) 459

[16] A high-resistivity carbon-filled epoxy paint manufactured by Abatron Inc., Gilberts, IL 60136, USA

[17] V. Steiner, PhD Thesis, Rehovot 1993

[18] R. Chechik and A. Breskin, Nucl. Instr. Meth. **A264** (1988) 251

[19] G. Lutz, W. Buttler, H. Bergmann, P. Holl, B.J. Hosticka, P.F. Manfredi and G.Zimmer, Nucl. Instr. Meth. **A263** (1988) 163

[20] Ch. Schwick, Diploma Thesis, Heidelberg 1990

[21] S. Tapprogge, Diploma Thesis, Heidelberg 1992

[22] B. Jähne, Digitale Bildverarbeitung, Springer 1989

[23] Th. Ullrich, Diploma Thesis, Heidelberg 1989

[24] J. Gläß, Diploma Thesis, Heidelberg 1990

[25] R. Baur, Diploma Thesis, Heidelberg 1990

[26] J. Gläß, R. Baur and R. Männer, IEEE Trans. Nucl. Sci. **NS-37** (1990) 241

R. Baur, J. Gläß and R. Männer, Computing in High Energy Physics, Tokyo 1991, Eds. I. Wanatabe and F. Abe, Frontier Science Series 3 (1991) 211

[27] R.A. Holroyd, J.M. Preses, C.L. Woody, R.A. Johnson, Nucl. Instr. Meth. **261** (1987) 440

[28] R. Arnold, Y. Giomataris, J.L. Guyonnet, A. Racz, J. Sèguinot, T. Ypsilantis, Nucl. Instr. Meth. **A314** (1992) 465

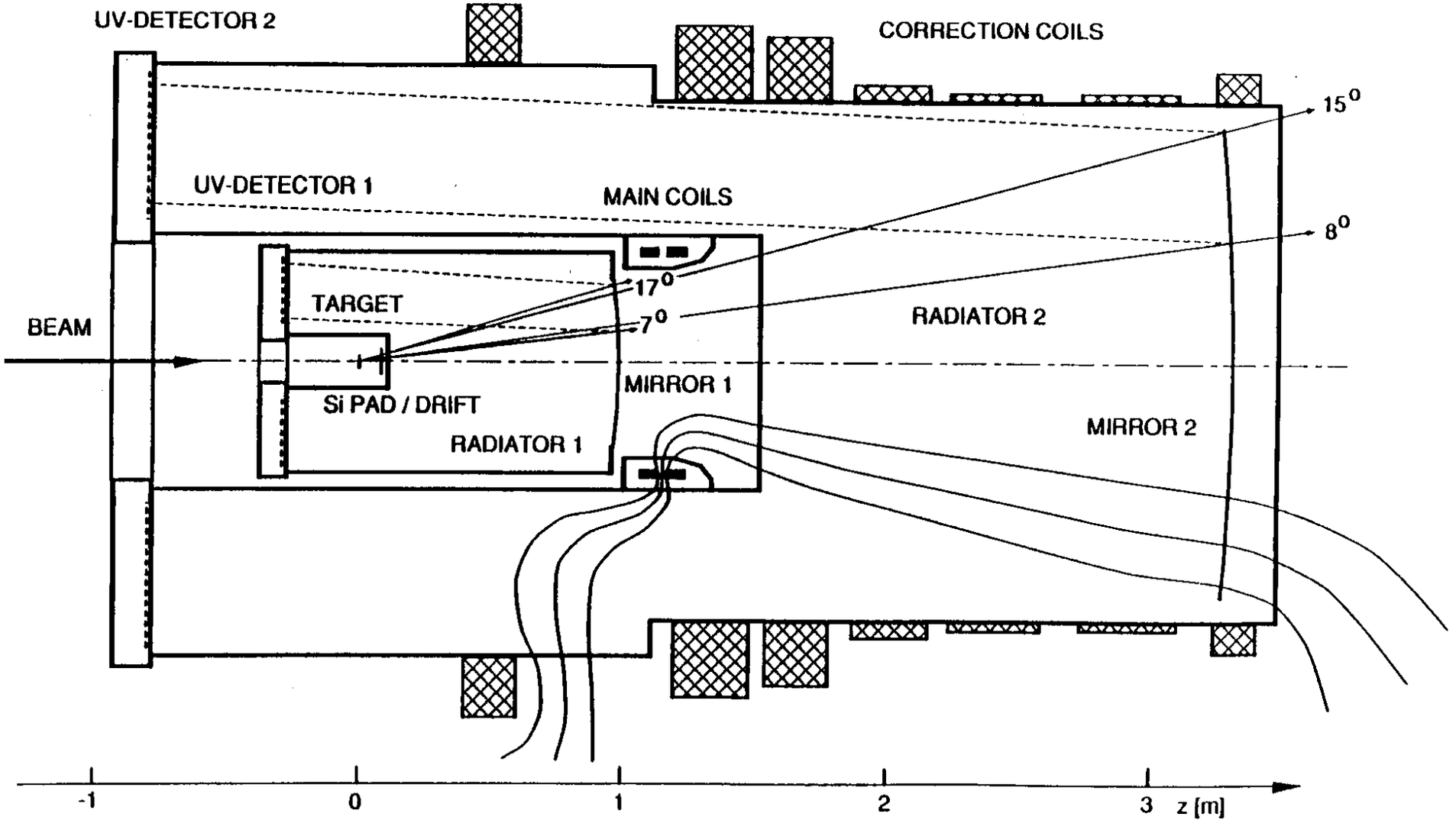
UV-DETECTOR 2
CORRECTION COILS
15°
UV-DETECTOR 1
MAIN COILS
8°
17°
TARGET
7°
RADIATOR 2
BEAM
MIRROR 1
Si PAD / DRIFT
MIRROR 2
RADIATOR 1
-1
0
1
2
3
z [m]

Fig. 1

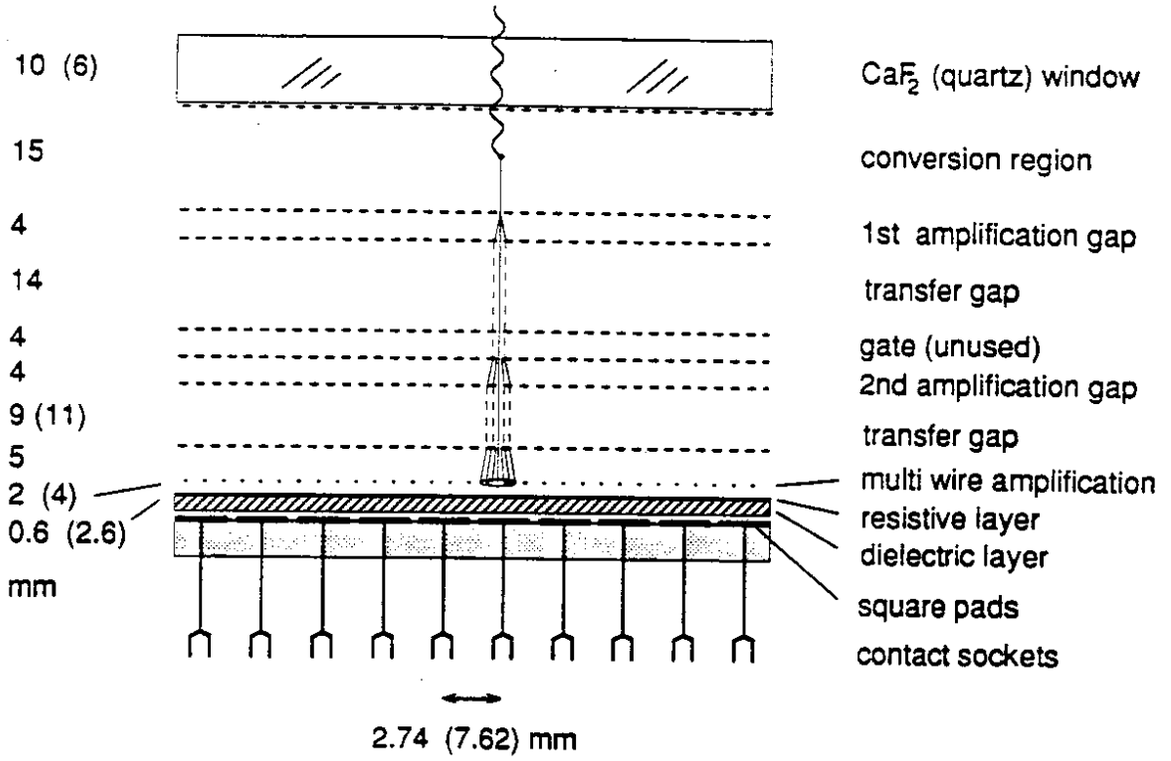
10 (6)
15
4
14
4
4
9 (11)
5
2 (4)
0.6 (2.6)
mm
CaF2 (quartz) window
conversion region
1st amplification gap
transfer gap
gate (unused)
2nd amplification gap
transfer gap
multi wire amplification
resistive layer
dielectric layer
square pads
contact sockets
2.74 (7.62) mm

Fig. 2

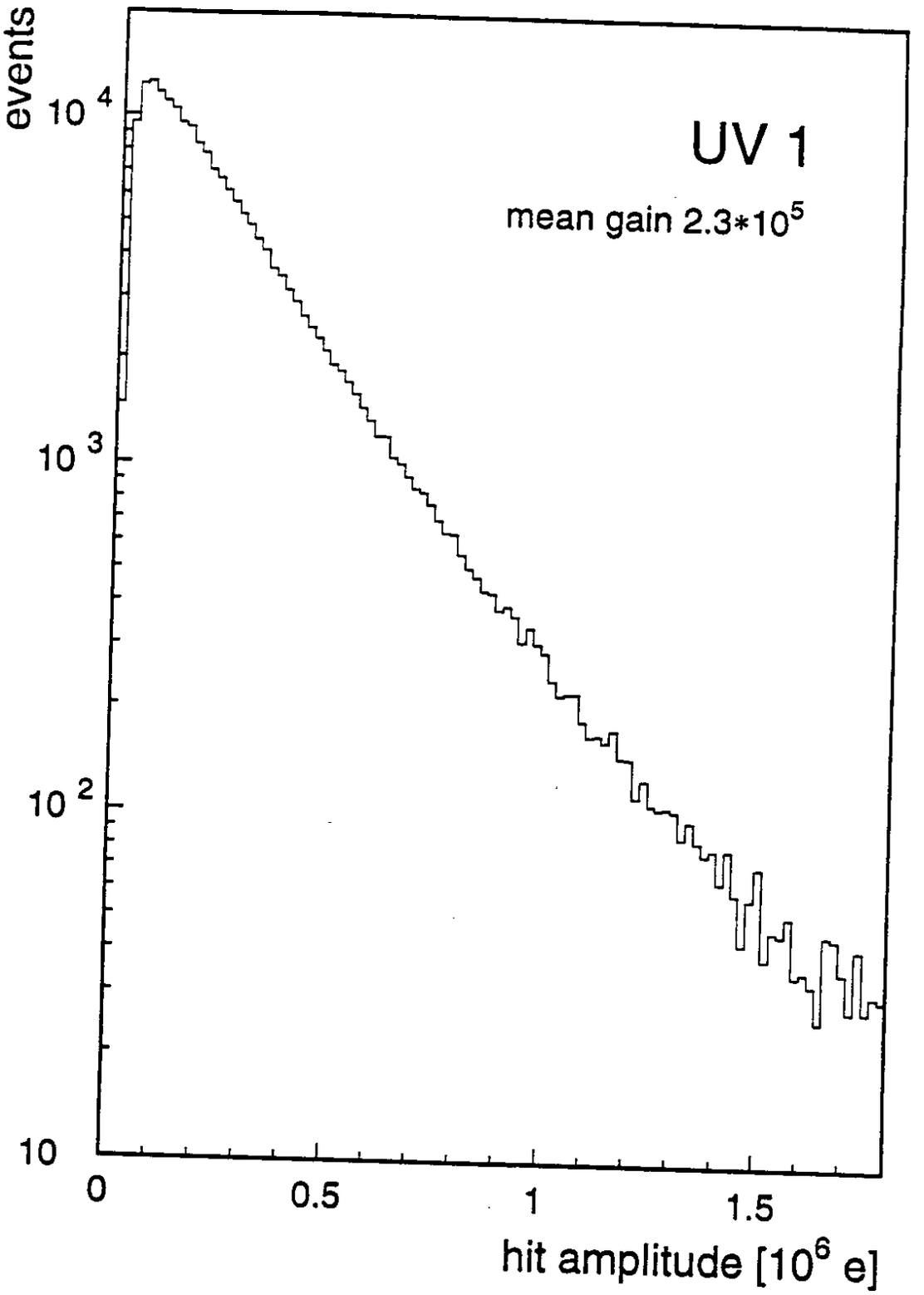
events
10 4
10 3
10 2
10
UV 1
mean gain 2.3*10^5
0
0.5
1
1.5
hit amplitude [10^6 e]

Fig. 3

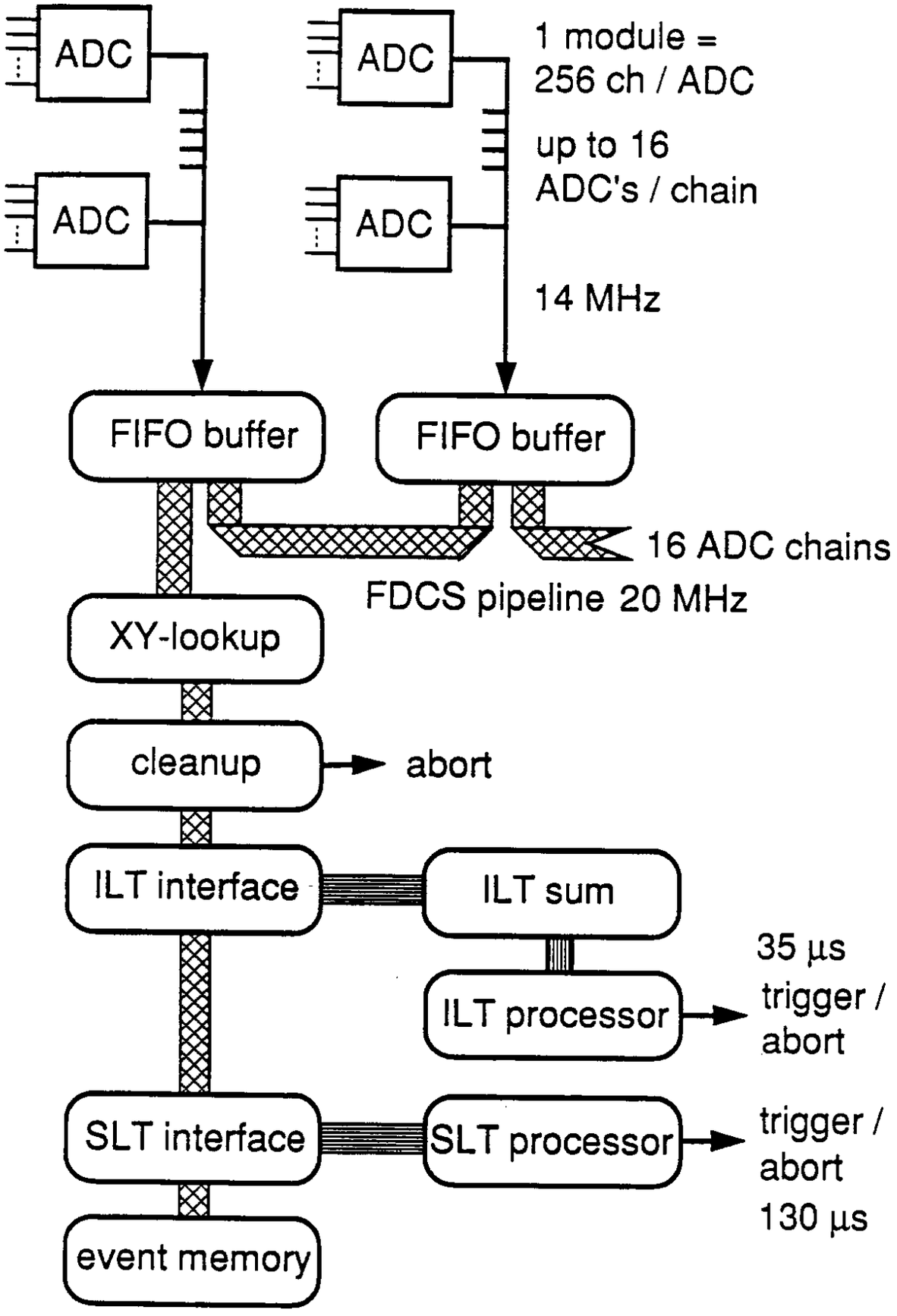
ADC
ADC
ADC
ADC
1 module =
256 ch / ADC
up to 16
ADC's / chain
14 MHz
FIFO buffer
FIFO buffer
16 ADC chains
FDCS pipeline 20 MHz
XY-lookup
cleanup
abort
ILT interface
ILT sum
35 µs
trigger /
abort
ILT processor
SLT interface
SLT processor
trigger /
abort
130 µs
event memory

Fig. 4

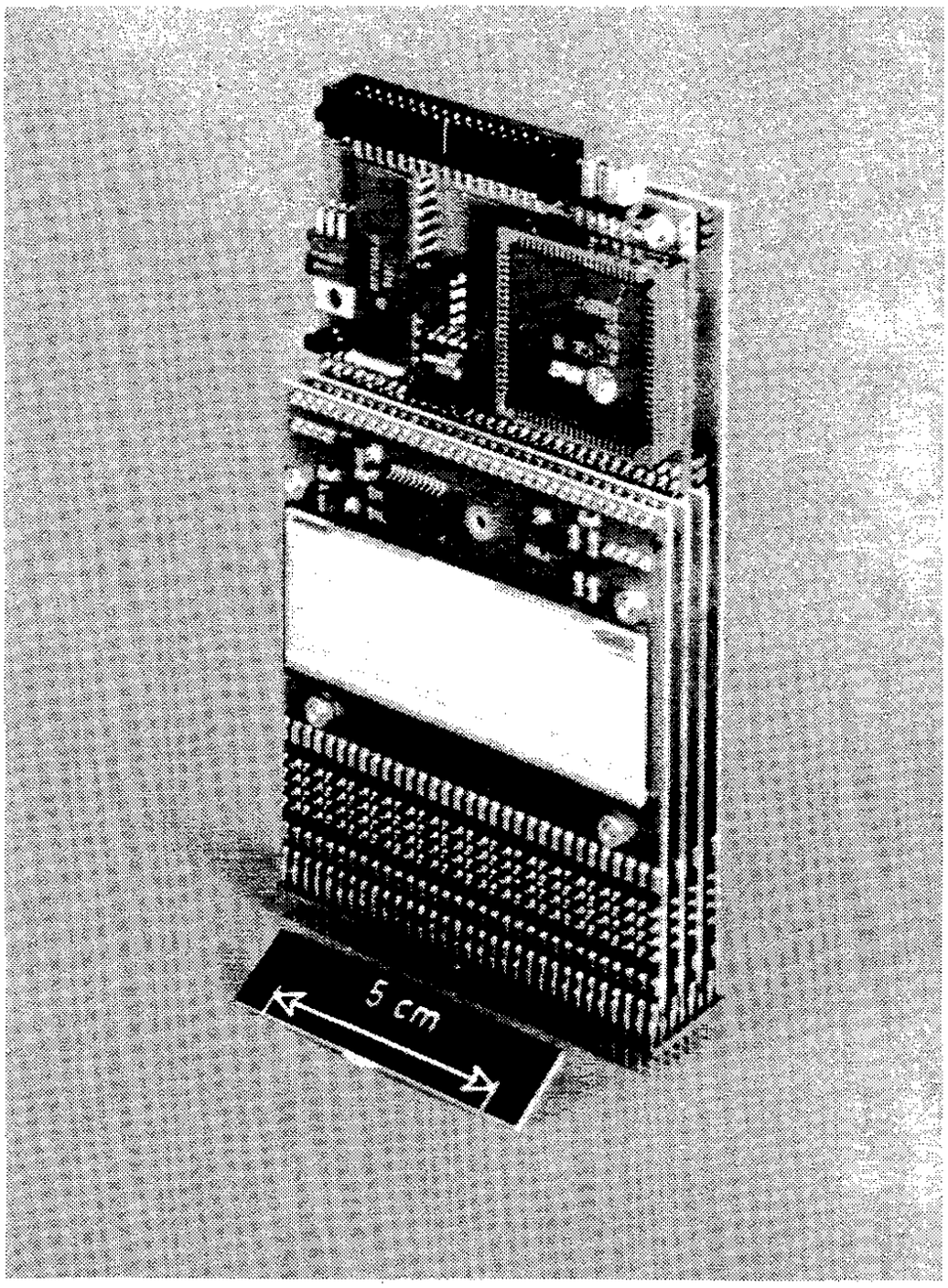

Fig. 5

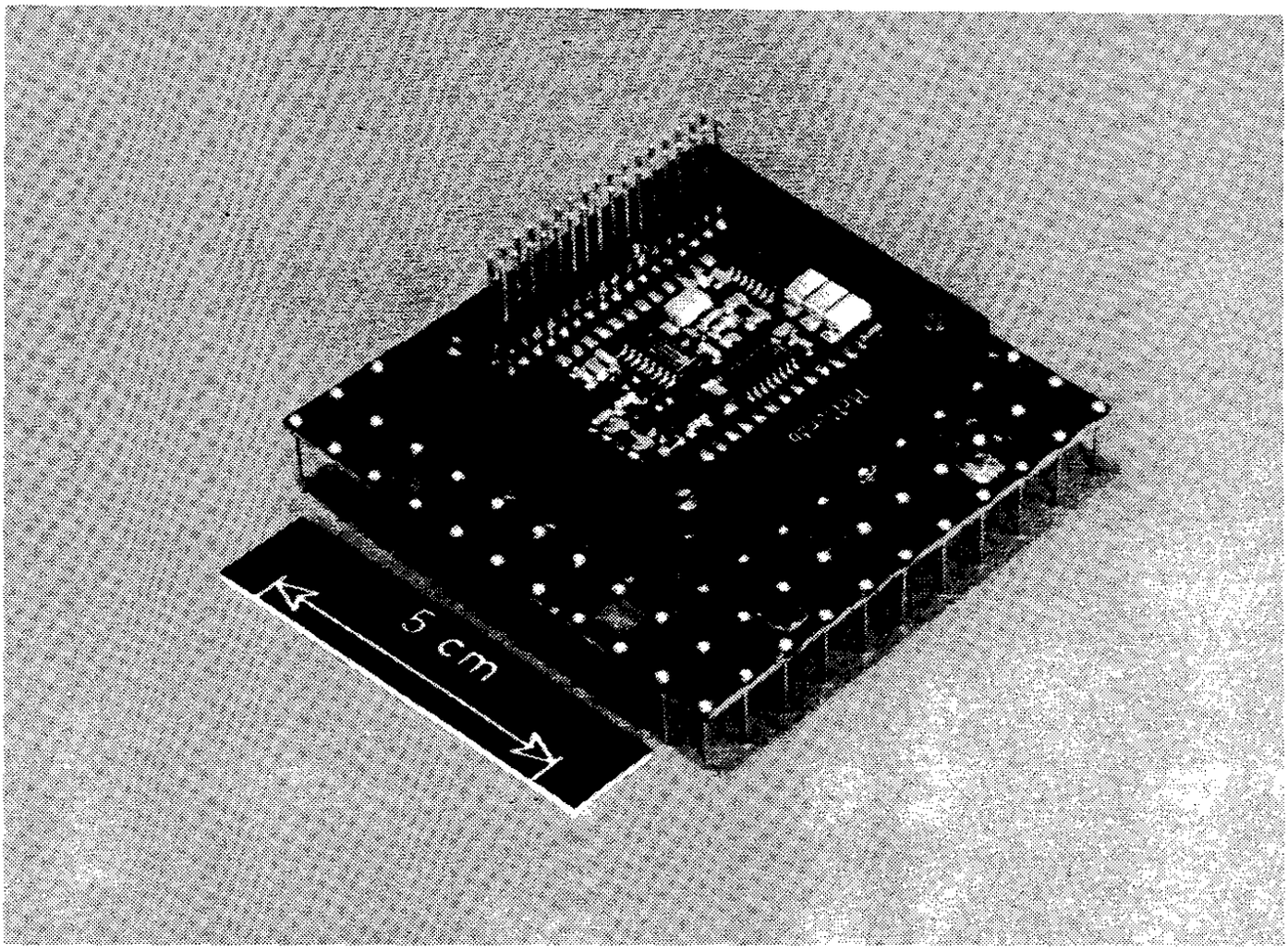

Fig. 6

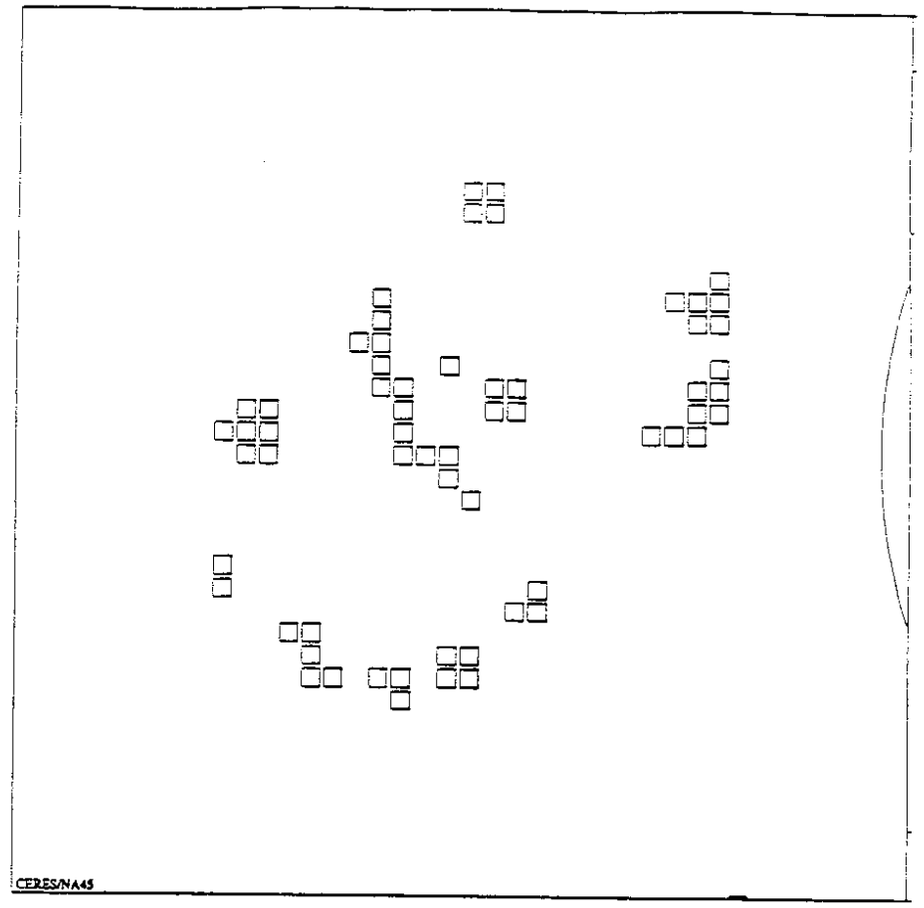

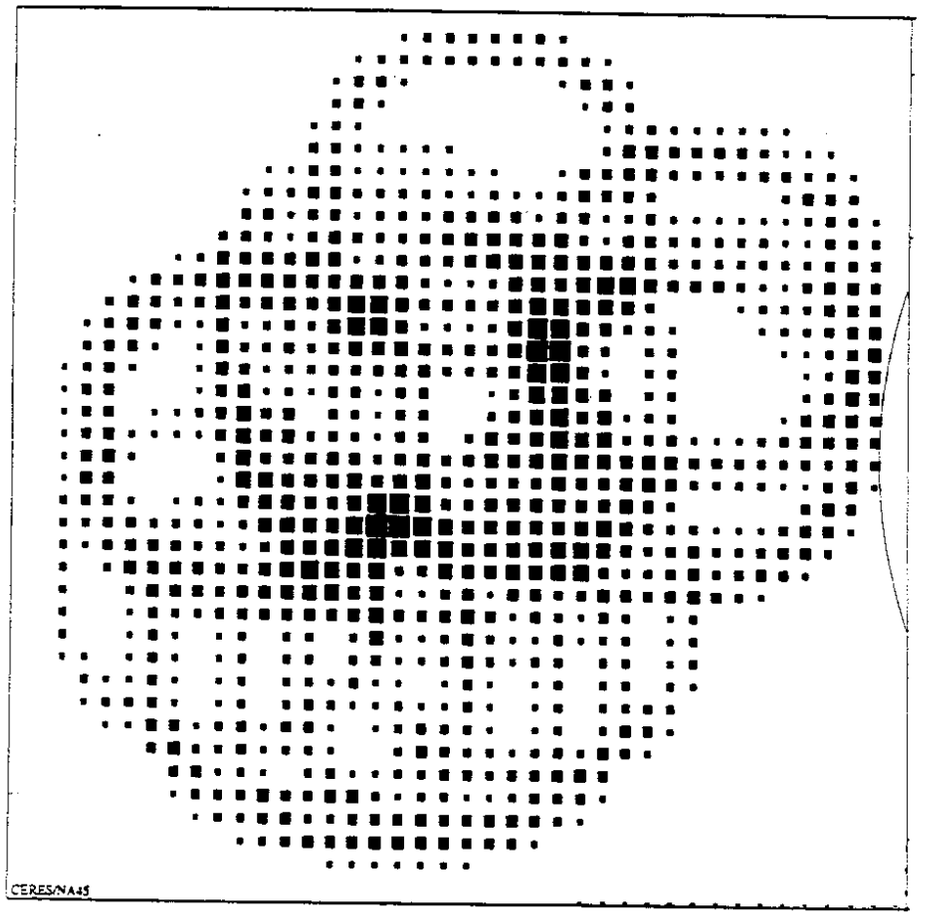

Fig. 7

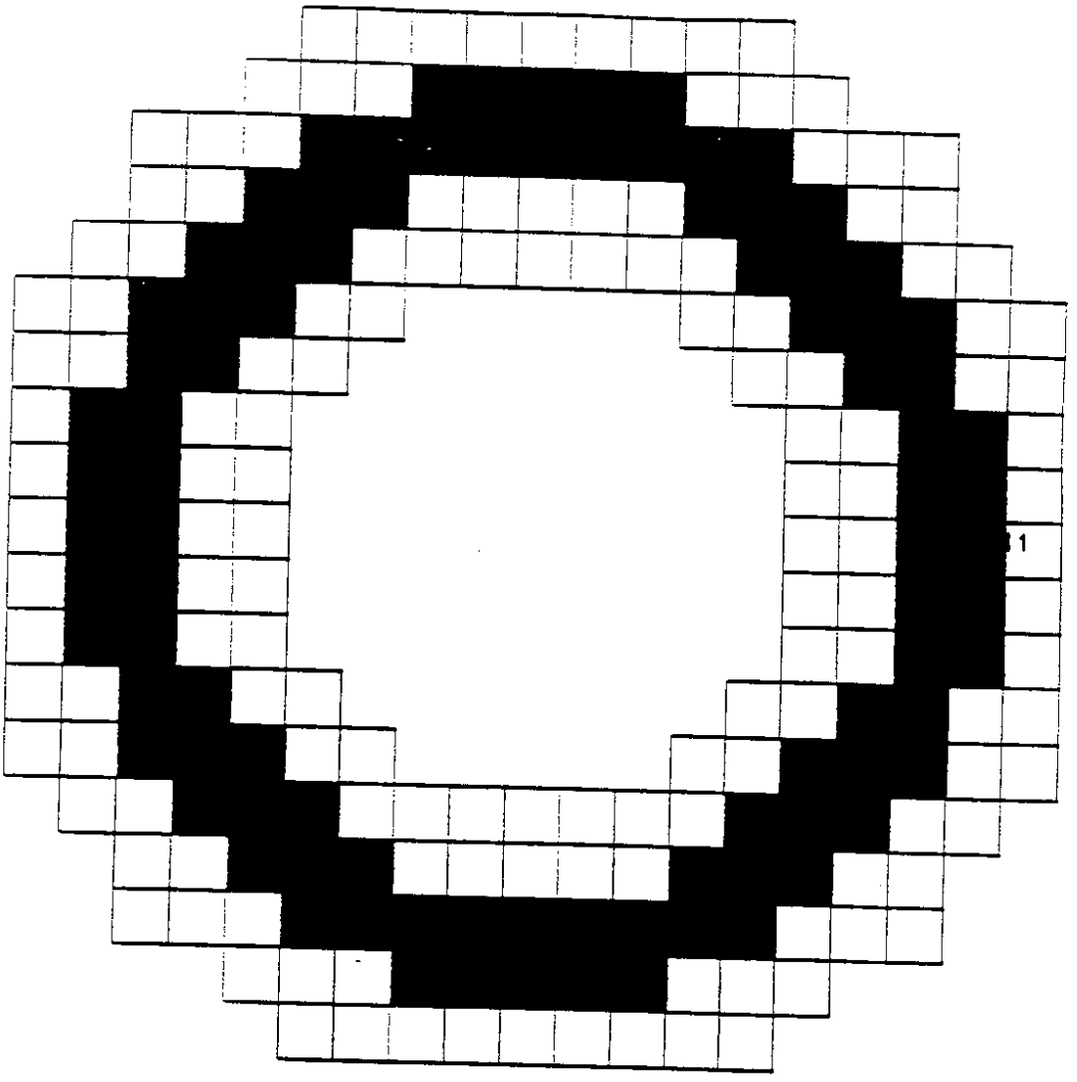

Fig. 8

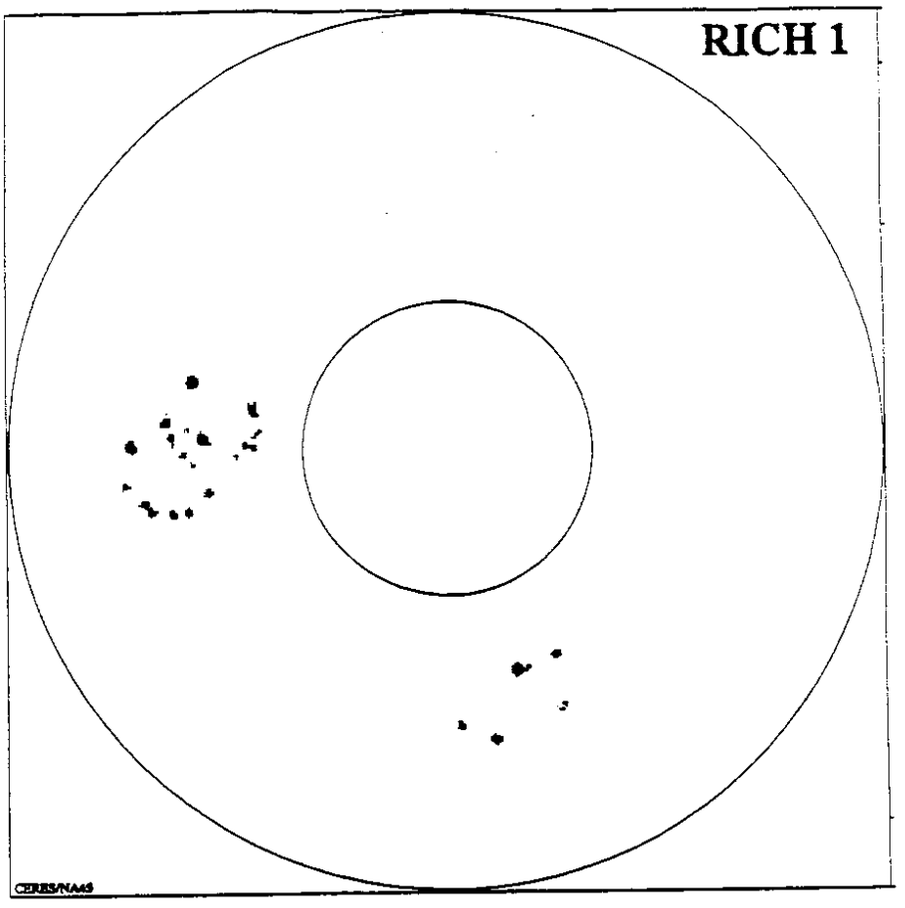

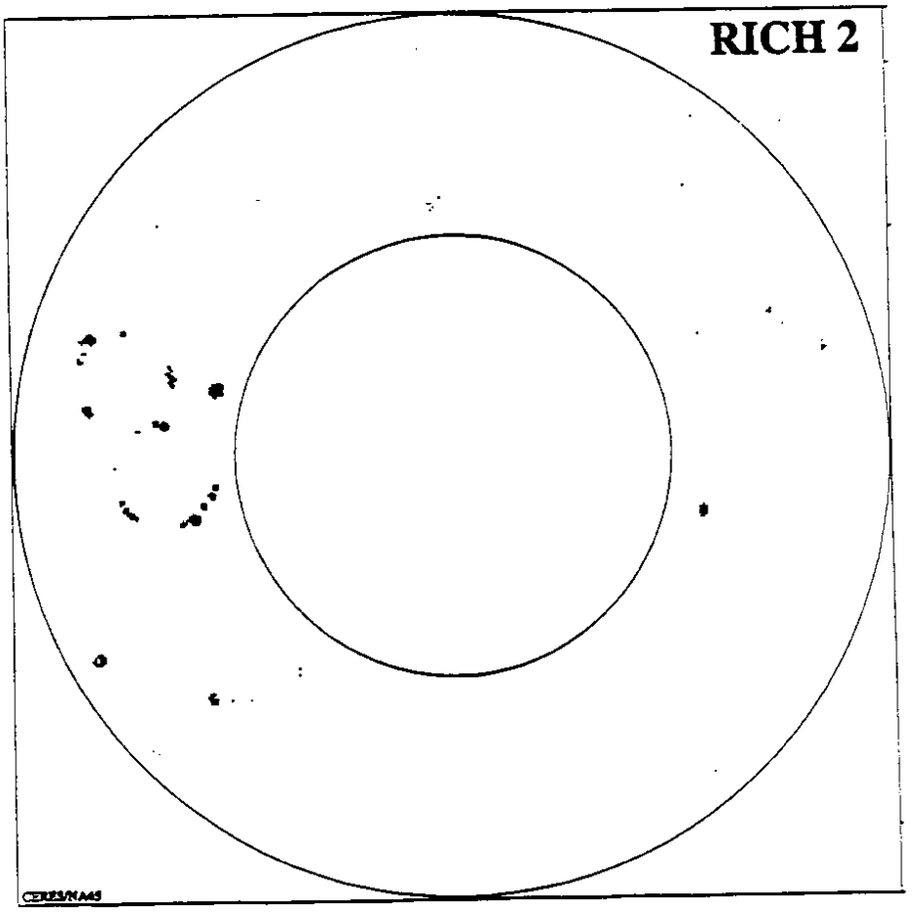

Fig. 9

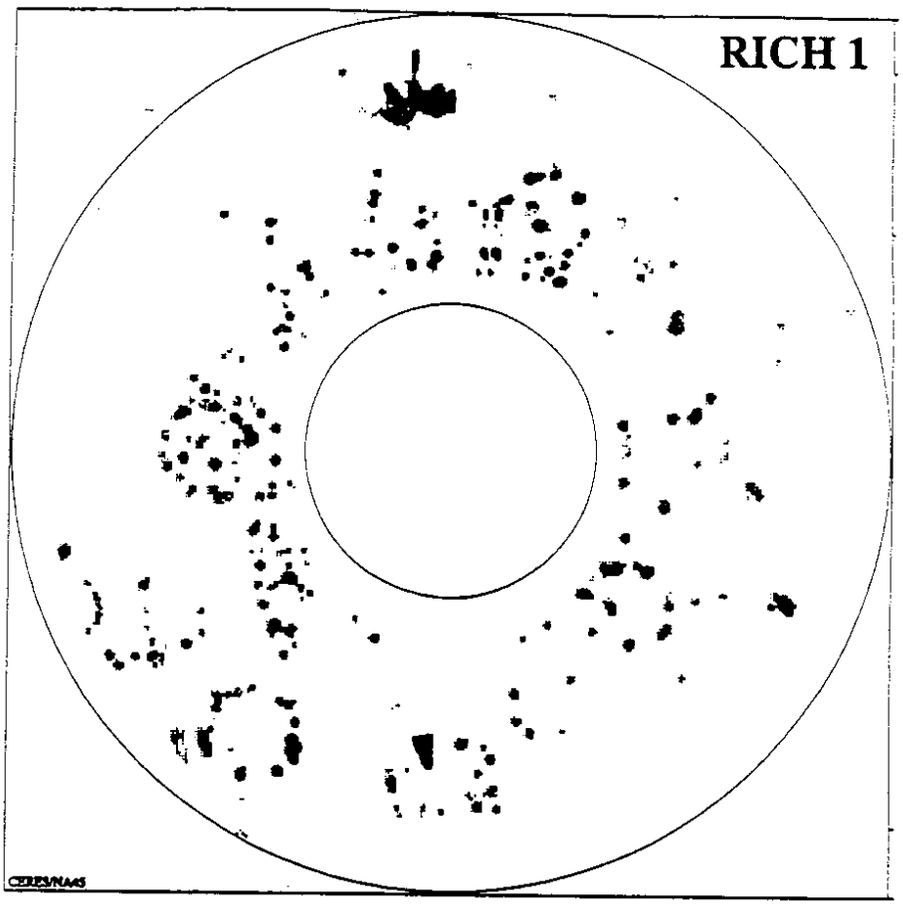

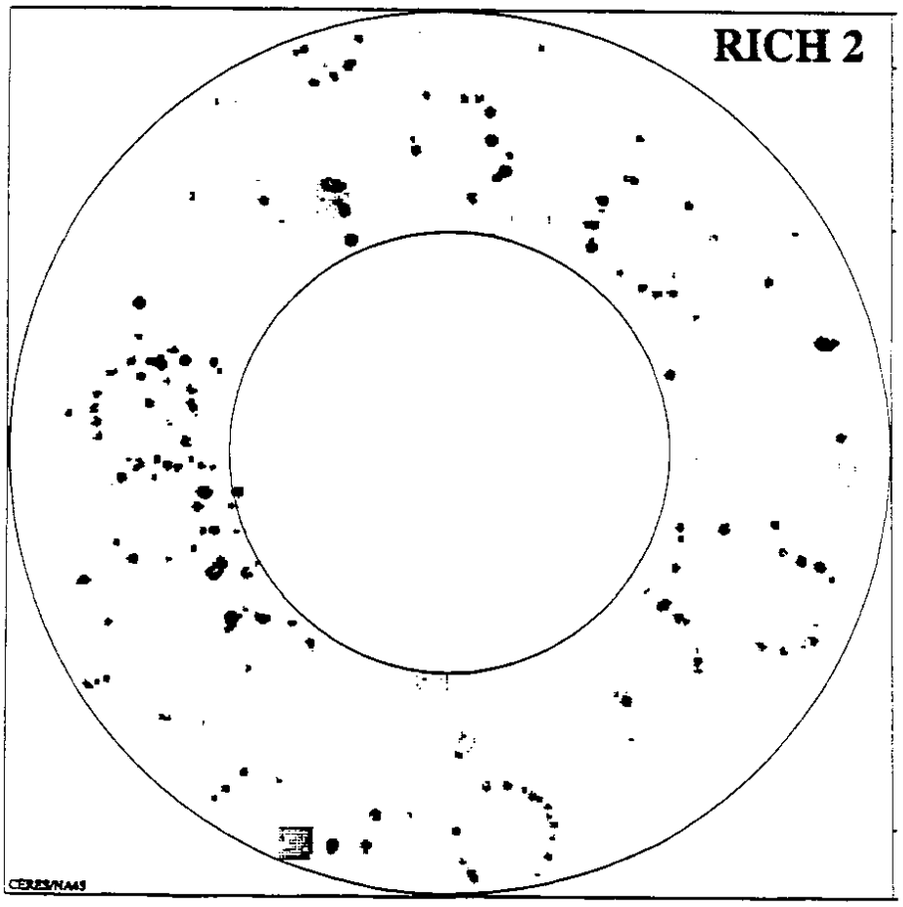

Fig. 10

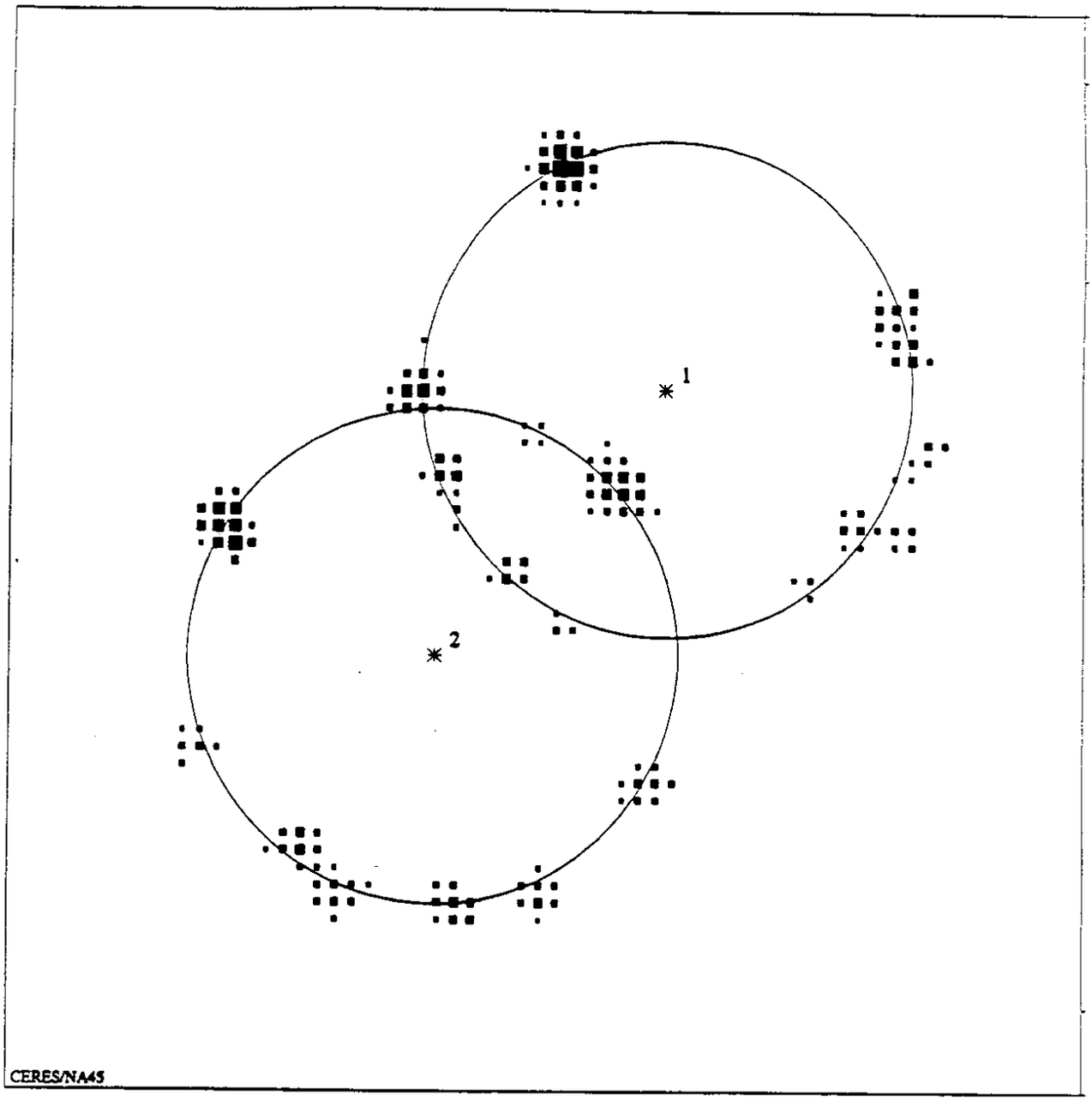

Fig. 11

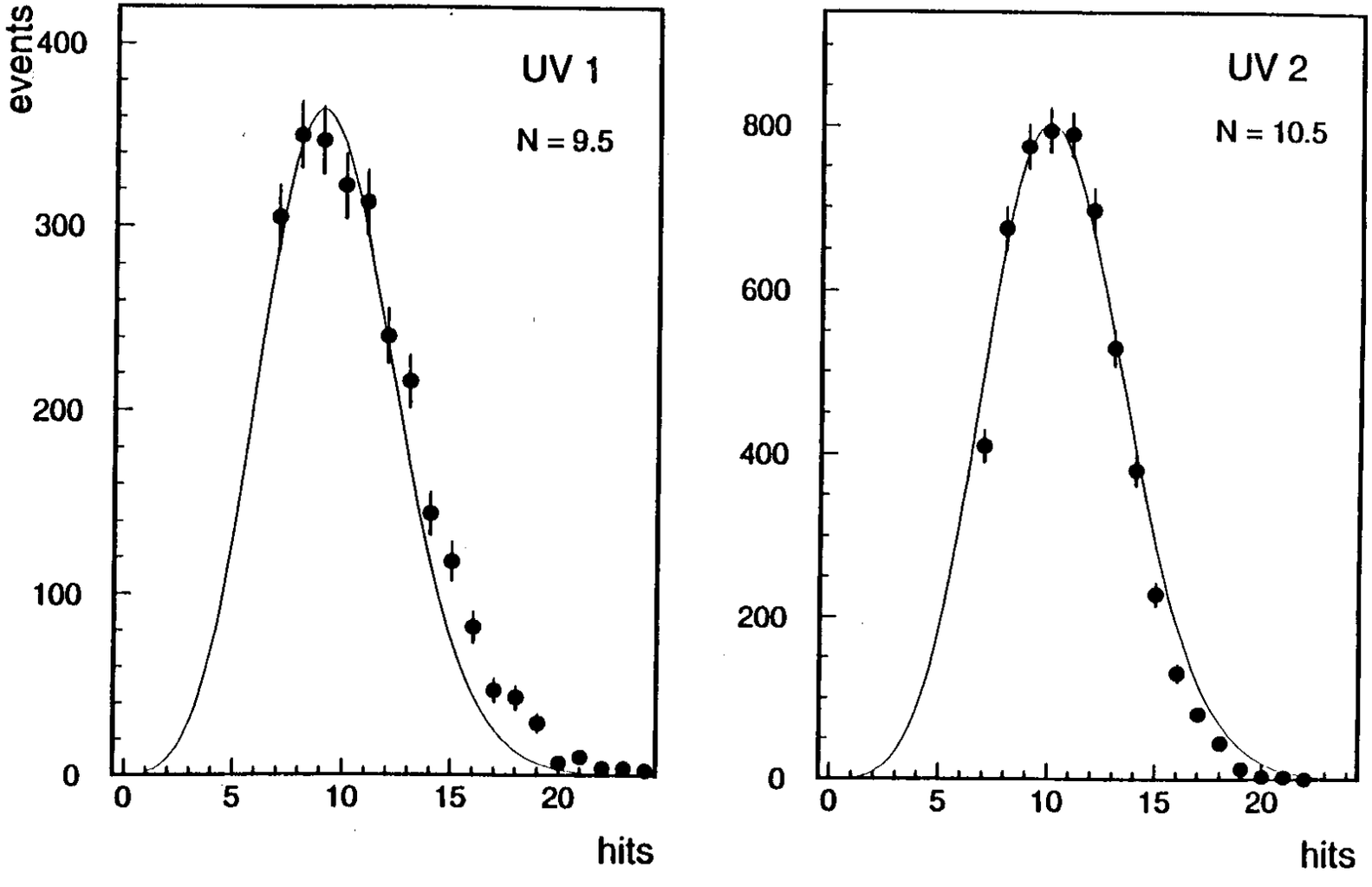
events
400
300
200
100
0
UV 1
N = 9.5
0
5
10
15
20
hits
800
600
400
200
0
UV 2
N = 10.5
0
5
10
15
20
hits

Fig. 12

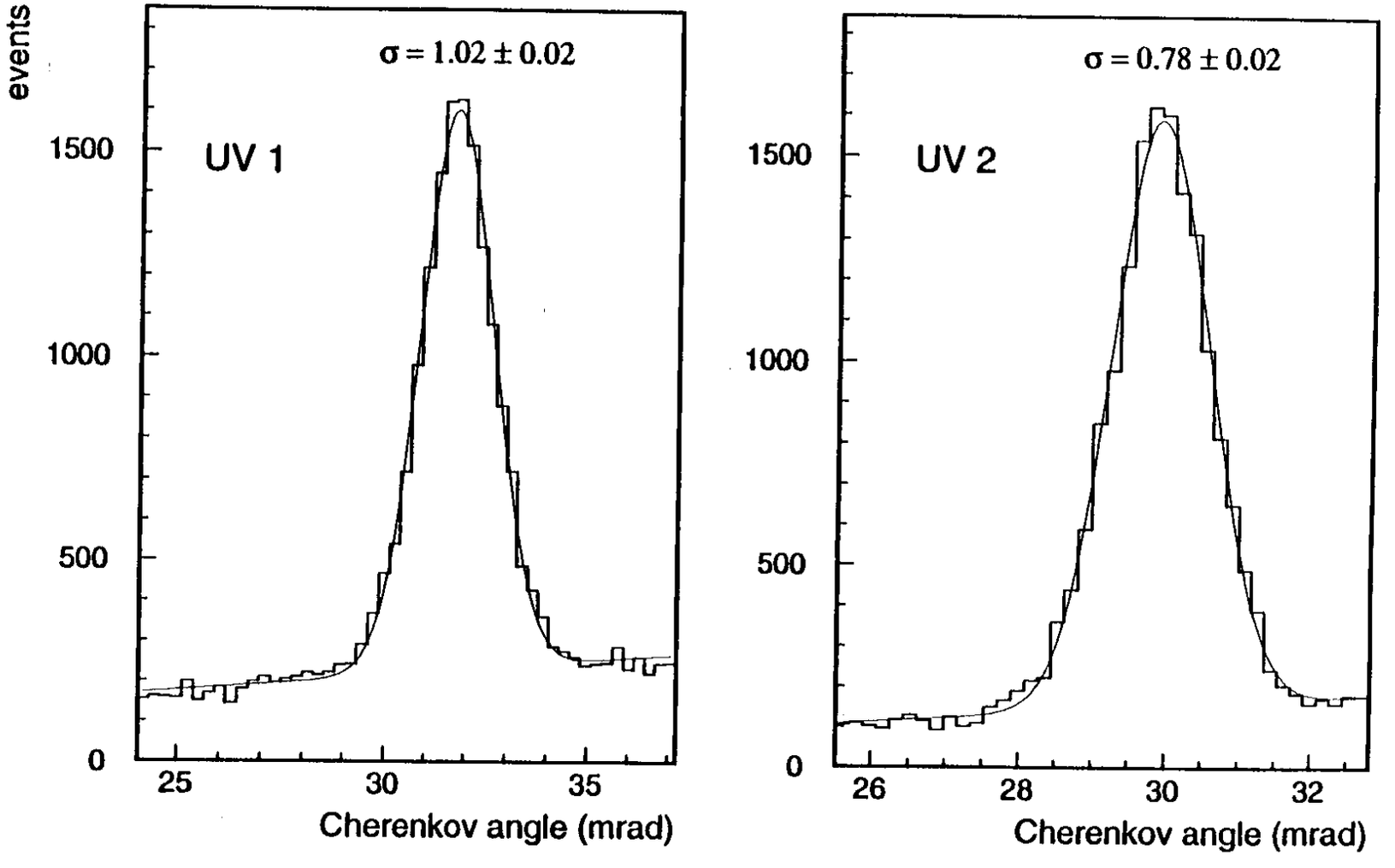

single-hit 22.8. pg

Fig. 13